NMR Imaging of Falling Water Drops

Song-I Han, Siegfried Stapf, and Bernhard Blümich
Lehrstuhl für Makromolekulare Chemie, ITMC, RWTH Aachen, Worringerweg 1, D-52074 Aachen, Germany
(Received 8 May 2001; published 17 September 2001)

The falling water drop is a simple model for studying phenomena related to chemical extraction, where two immiscible phases are dynamically blended to promote the transport of solute molecules from one phase to the other. Convective motion inside the drop significantly influences the extraction efficiency. Whereas optical and tracer methods are model bound or invasive, NMR imaging is noninvasive, direct, and applicable to nontransparent media. The first NMR measurements of a water drop falling through air are reported. It is shown that, in drops from pure water, large-scale convection rolls are observed in contrast to drops with the surface tension lowered by surfactants.

DOI: 10.1103/PhysRevLett.87.144501 PACS numbers: 47.55.Dz, 47.32.Cc, 68.03.Cd, 82.56.Fk

Chemical extraction is a fundamental process in the purification of chemical compounds. Typically drops of one phase are bubbled through a second, continuous phase. The size of the contact surfaces and the transport of solute molecules to the interface are crucial parameters in the extraction process. Apart from being of fundamental interest, the falling drop is the simplest model for studying extraction phenomena. Nevertheless, the dynamics of moving drops remain a challenge for scientists [1–7]. Falling drops are investigated, e.g., by optical methods, where the shape is interpreted in terms of fluid dynamic models [8,9]. More directly but invasively, convective motion can be studied by particle tracers techniques [10–12]. NMR is suitable for noninvasive mapping of velocity distributions even in nontransparent drops [13,14] as long as identical drops can be generated repetitively over a longer period.

In this work, water drops with and without surfactant (2.8% betaine) were generated at a frequency of about one per second by maintaining a constant filling height above a glass pipette with a high precision pump, and were allowed to fall free through air. The experimental setup consisted of this glass pipette mounted in a long glass tube inside a 4.7 T vertical bore magnet equipped with a Bruker DSX-200 spectrometer, and an infrared photosensor placed 30 mm below the tip of the pipette, which triggers the spectrometer each time the drop obstructs its light path. The center of a bird cage resonator was located about 200 mm below the tip of the pipette; hence a falling velocity of about 2 m/s results, and the drop remains within the sensitive volume of the bird cage resonator only for about 10 ms. As a consequence, any ultrafast NMR imaging method is incapable of completing the measurement within the residence time of a single drop; the available time of 10 ms allows one to acquire no more than one NMR echo per drop, whereby echo and acquisition times as short as possible are desirable for all measurements to avoid motional blurring. Using triggered cyclic acquisition was the only possibility for signal accumulation as well as for making multidimensional experiments feasible. Because every single scan had to be collected from a different drop, the uniformity in the shape of each drop over an experimental time up to several hours are indispensable conditions for reliable NMR experiments. Otherwise, random contributions would lead to a partial extinction of the accumulated signal. The uniformity of the dripping process was proven by various NMR imaging methods. The challenge of applying NMR imaging methods to a free-falling water drop is its fast-falling velocity, and the fact that at the "moderate" velocity of 2 m/s, which has been realized in the presented experiments, the drop did not reach a stationary state, which prevails at approximately 10 m/s, i.e., the drop still experiences accelerated motion. To meet this challenge, short gradient encoding times of about 0.2 ms were chosen, so that motional blurring is minimized and the effect of acceleration can be neglected.

Any magnetic field gradient $\vec{G}(\vec{r}) = \vec{\nabla} B_z$ generated in the static magnetic field $\vec{B}_0$ has the effect of producing a magnetic field component in addition to the static magnetic field $\vec{B}_0$ which leads to an encoding of position $\vec{r}$ via the relation of the Larmor precession frequency, $\omega_L(\vec{r}) = \gamma|\vec{B}_0| + \gamma\vec{G}(\vec{r}) \cdot \vec{r}$, where γ is the gyromagnetic ratio. This information can be exploited directly by signal acquisition in the presence of the gradient field, where the spin density is obtained by Fourier transformation of the echo signal from the time domain into the frequency domain (frequency encoding method), or by Fourier transformation of many echoes following short gradient pulses, which lead to a phase shift of the signal of each position-dependent spin isochromat (phase encoding method) [13–16].

One-dimensional projections of the falling drop were repeated by measurements employing the frequency encoding method with different numbers of accumulations along all three spatial dimensions. The 1D profiles resulting from 1, 2, 3, and n accumulations, i.e., being collected from as many different drops as the number of accumulations, differed only in their amplitude, which was found to be strictly proportional to the number of accumulations. The variance calculated between profiles from several experiments was less than 1%, thus setting an upper bound for

 © 2001 The American Physical Society

the random variation of the drop formation. In a subsequent step further 1D profiles were measured by the phase encoding method for comparison, where each data point is obtained by incrementing the amplitude of the gradient pulse in a triggered cycle so that as many drops as the number of image pixels times the number of accumulations constitute the signal, which renders the density profile after Fourier transformation. Excellent agreement of the profiles obtained by both methods was found in all three spatial directions. The profiles reproduced the drop diameter, proving the uniform dripping behavior with a deviation of less than 1%. The equivalence of the results from frequency and phase encoding experiments further demonstrates the complete interchangeability of both methods despite their inherently different susceptibility to motion during the imaging sequence [16]. It can thus be concluded that distortions of position information due to motion artifacts can safely be neglected. Furthermore the results of the test experiments prove the applicability of a wide range of multidimensional NMR imaging experiments to the falling drop, provided that they can be performed by employing a short echo time of a few milliseconds.

The surface tension of the fluid is expected to be a crucial factor, dominating the shape and dynamics of a drop. In this paper, one set of drops of an aqueous surfactant solution and two sets of water drops (indicated as I, II in the figures) are discussed. Figure 1 presents 3D spin density images of a falling drop consisting of 2.8% aqueous betaine solution [1(A)] and pure water [1(B) and 1(C)]. The images were acquired by combining frequency encoding in one direction and phase encoding in the remaining two spatial directions. Considering that one 3D experiment takes about 10 h and a total of 33 800 drops constitute the NMR signal, the quality of the 3D images obtained after Fourier transformation is excellent.

The coordinate system used in the following discussion is given in Fig. 1(A), where z is the vertical and x, y are the transverse directions relative to the gravity axis. The images 1(A)–1(C) are surface rendered representations, and images 1(D)–1(F) are their corresponding projections onto z presented as contour plots. As expected, the decrease of the surface tension obtained from adding surfactants leads to a reduction in drop size from $\text{Ø} = 3.6$ to 2.8 mm. At the same time, both the shape of the drops and its reproducibility are affected: the surfactant solutions form a spherical drop [Figs. 1(A) and 1(D)], which has been shown to be fully reproducible in shape and size for different sets of experiments. In the case of pure water, on the other hand, once the dripping process has started, identical drops are produced, but the drop shape deviates from a spherical geometry and varies from one series to another [Figs. 1(B), 1(E) and Figs. 1(C), 1(F)]. Because of the large surface tension of water, water remains for a longer period on the edge of the glass pipette before the drop formation is completed. This results not only in a drop diameter larger than for the surfactant solution but also in a critical dependence of the drop shape on experimental conditions, such as small impurities on the surface, shape imperfections, and the alignment of the pipette relative to the gravity axis. The difference in the drop shape of water and the surfactant solution already indicates different internal drop dynamics. The Reynolds numbers of the drops were 470 for water and 360 for the surfactant solution. Both numbers are well outside the regime of stationarity and laminar conditions. They are determined as $\text{Re} = v_d(d_d/\nu_c)$, where v_d is the falling velocity of the drop, d_d is the drop diameter, and

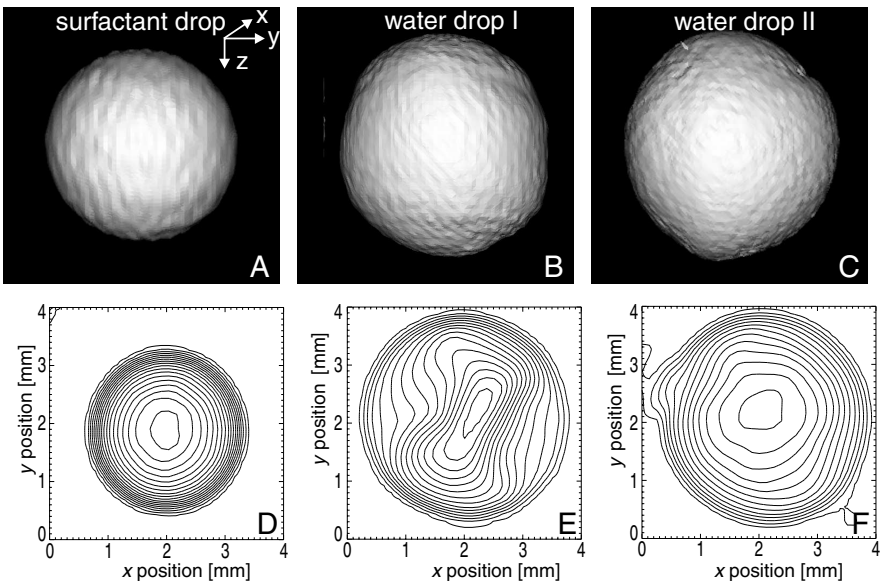

FIG. 1. Three-dimensional NMR spin density images of falling drops of 2.8% aqueous betaine solution [(A), (D)] and pure water [(B), (E), and (C), (F)]. (A)–(C) Surface rendered representations. (D)–(F) Contour plots of the spin density projected onto the xy plane normal to the gravity axis z. The lines represent 15 equidistant levels of the spin density, where points of the same values are connected.

ν_c is the kinematic viscosity of the continuous phase [2,3]. The flow regime of the dynamics of moving drops can be divided by the Reynolds number into creeping laminar, stationary laminar, and turbulent regimes, which are defined by an interplay between the inertial effect of the drop and the viscous effect of the continuous phase.

Although the outer shape of the drop allows one to draw some conclusions about the dynamics, the large potential of NMR imaging is more fully exploited by measuring directly the velocity field of the drop in different spatial directions. Spatial distributions of velocities within the drop have been analyzed, acquiring 2D projections along the cross section of the drop, where the NMR phase ϕ of the signal encodes either the vertical (v_z) or transverse (v_x) velocity component. For phase encoding of velocity a standard pulsed field-gradient pair with amplitude G, duration δ, and time separation Δ was used so that $\phi = \gamma\delta G v \Delta$ [13]. Figures 2(A)–2(C) show the distributions of v_z along the xy plane and Figs. 2(D)–2(F) show the distribution of v_x along the zy plane of the drop. For the drop of surfactant solution, the distributions of v_z [2(A)] as well as of v_x [2(D)] reveal small-scale variations. The fact that the averaged transverse velocity amounts to zero excludes the contribution of any net motion of the drop itself in the transverse direction. The existing variance of v_x between $+2$ mm/s and -2 mm/s can be attributed to fluctuations or small-scale vortices. The average of the v_z distribution amounts to the expected falling velocity of 2.0 m/s, superimposed with a variation of ± 0.04 m/s. This is still a small fluctuation compared to the net motion, but 20 times larger than the variation in v_x. The v_z [2(B) and 2(C)] and v_x [2(E) and 2(F)] distributions in falling water drops show characteristics fundamentally different from those of the surfactant drop. Large-scale structures in the velocity distribution and larger variations are common to all four images. Although the two series of water drops [2(B)and 2(E) versus 2(C) and 2(F)] differ from each other, both series have a net transverse velocity of zero and an average falling velocity of 2.0 m/s, in agreement with the behavior of the surfactant drop, but with a broader velocity distribution with a full width half maximum of 0.3 m/s. Excluding net transverse motion of the drop itself, the marked structures in the v_z and v_x distributions can be attributed to large-scale motion inside the drop. In Fig. 2(B), two pronounced holes are symmetrically placed relative to the center on the xy plane. Although Fig. 2(C) is different from Fig. 2(B), the depression of the v_z signal on two opposite sides of the drop plane is a common feature as well as the elevation of v_z intensity in between. Because an upstream motion results in a reduced v_z value, the depression can be explained by the presence of at least one pair of convection rolls with their upstream motion placed on the position of the holes and their downstream motion in between. Whereas the structure in Fig. 2(C) can be interpreted by one pair of large convection rolls along the z direction in the drop, the increase of velocity at the edges observed in Fig. 2(B) indicates the presence of more complex motion. This marked behavior goes along with a larger deformation of the drops from spherical shape [Figs. 1(B) and 1(E)]. In Figs. 2(E) and 2(F) the distribution of transverse velocity in the projection onto the zy plane is presented. The unambiguous information which can be derived from the v_x distribution is its net velocity of zero, which proves that the structure is likely to originate from large-scale motion. Evidence for the presence of convection rolls was already given in the discussion of the v_z distribution, but Figs. 2(E) and 2(F) indicate that additional large-scale oscillations of the drop shape should be considered as well. Such

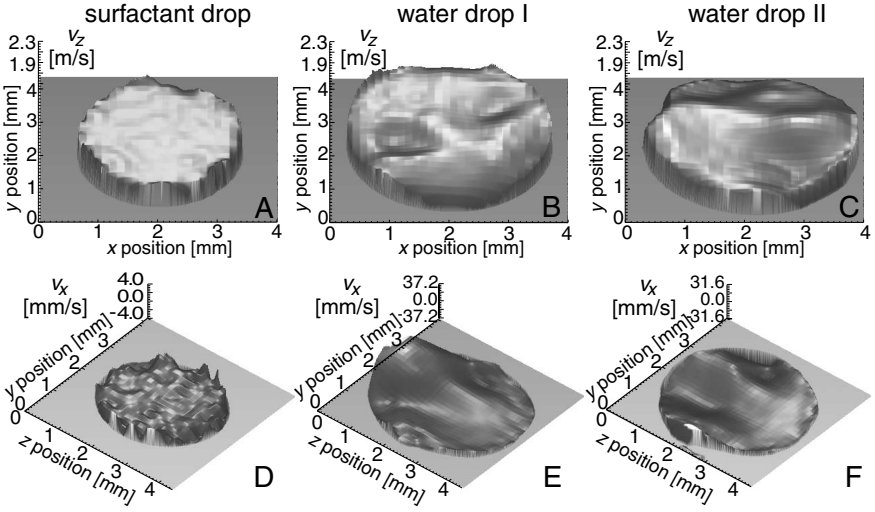

FIG. 2. (A)–(C) Velocity component v_z as a function of position in the xy plane, averaged over the z dimension of the drop. (D)–(F) Velocity component v_x as a function of position in the zy plane, averaged over the x dimension. The labels (A)–(F) are assigned in agreement with Fig. 1. Each figure of (A)–(C) reveals a falling velocity of 2.0 m/s, whereby the variance of (A) (0.04 m/s) is much smaller than that of (B) or (C) (0.3 m/s). Similarly (D) shows a much smaller variance (2 mm/s) than (E) or (F) (30 mm/s). It is concluded that drops of distilled water reveal not only large-scale structures in their spatial distribution of velocities but also larger variances of velocity values compared to drops of the surfactant solution.

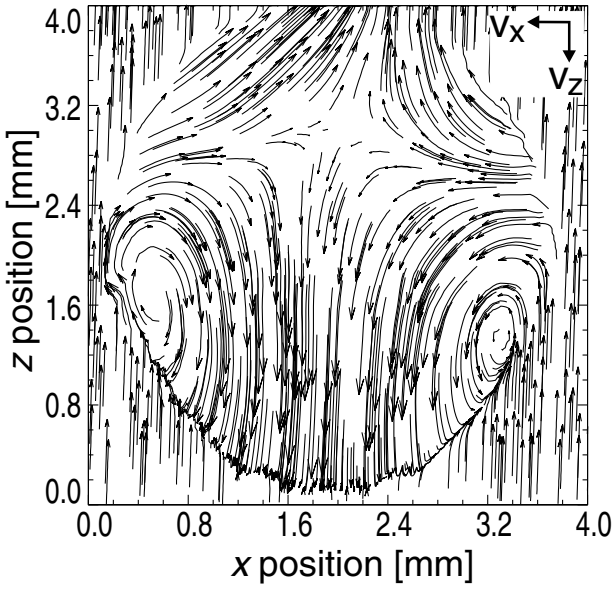

FIG. 3. Velocity components v_z, v_x for a drop of pure water falling at 2.0 m/s as a function of the position along the zx plane, averaged over the y dimension of the drop. The magnitudes of the velocities are indicated by the lengths of the arrows. The v_z component is scaled relative to the average falling velocity of 2.0 m/s. A pair of vortices is readily identified.

oscillations add their contributions to the velocity field of the drop motion and result in even more complex dynamics, which can be expected for such high Reynolds numbers. Although the unambiguous interpretation of the observed velocity field in terms of a simple convection pattern is not possible from those data, a net variation in the velocity field means a net average velocity v_x in the x direction, which is different from zero in each pixel of the zy plane. It should be noted that, even for the largest velocity components measured, the total change in drop shape during the data acquisition time is still negligible. Large oscillations therefore represent no contradiction with the notion of a reproducible drop shape, because due to the short gradient encoding times the maximum amplitude of oscillatory motion during the measurement time of the drop shape is below 0.1 mm.

A much more direct way to visualize internal fluid dynamics is to measure both the v_z and v_x components in each pixel of the zx plane simultaneously within a single experiment and to combine this information into a vectorial representation. Such experiments are time consuming because two 3D measurements containing two spatial and one velocity dimensions have to be completed within one experimental run lasting about 18 h. Because water drops evidently contain large-scale dynamics in contrast to the surfactant drop, they remain the object of our interest. This experiment was performed on the second series of the water drops (II). The vector plot (Fig. 3) clearly reveals the presence of stable vortices within the drop. Because the measured signal is from water and not from the surrounding air, and the velocity components are plotted relative to the average falling velocity of 2.0 m/s, the velocity vectors outside the drop indicate the negative falling velocity and help to visualize the motion inside the drop. In addition to two vortices right and left in the drop, a node is observed in the upper center. It is explained by an additional oscillatory motion, which had been confirmed by optical methods to last a few seconds, i.e., much longer than the 205 ms, which passed in the lifetime of the drops until their observation by NMR.

These investigations demonstrate that NMR is capable of directly measuring the internal velocity pattern of a free-falling drop. The presence of large-scale convection rolls was confirmed and visualized directly. NMR imaging appears to be the only technique able to acquire *in situ* internal dynamic information from free-falling drops in a noninvasive and direct way. This work establishes the basis for comprehensive NMR studies with the ability to reconstruct the three-dimensional structure of the inner vortex and oscillation dynamics in falling drops and related flow phenomena. Considering the ability of NMR imaging to access chemical shift information, these investigations can be expanded towards chemically selective analysis of transport characteristics in multicomponent systems within and outside a drop.

This work was funded by DFG as part of SFB 540. We thank Dr. Peter Blümler who proposed this work and Dr. Martin Henschke for discussion and helpful suggestions. The people from the electronic workshop are acknowledged for setting up the trigger electronics.

[1] A. M. Worthington, *A Study of Splashes* (Longmans, London, 1908).
[2] H. R. Pruppacher and K. V. Beard, Q. J. R. Meteorol. Soc. **96**, 247 (1970).
[3] B. P. LeClair *et al.,* J. Atmos. Sci. **29**, 728 (1972).
[4] M. J. P. Nijmeijer *et al.,* J. Chem. Phys. **96**, 565 (1992).
[5] B. Brander and H. Brauer, *Reihe 3: Verfahrenstechnik* (VDI-Verlag, Düsseldorf, 1993).
[6] P. H. T. Uhlherr and R. P. Chabra, Can. J. Chem. Eng. **73**, 918 (1995).
[7] M. P. Brenner *et al.,* Phys. Fluids **9**, 1573 (1997).
[8] E. A. Hauser, H. E. Edgerton, and W. B. Tucker, J. Phys. Chem. **40**, 973 (1936).
[9] H. E. Edgerton, E. A. Hauser, and W. B. Tucker, J. Phys. Chem. **41**, 1017 (1941).
[10] J. C. Hunter and M. W. Collins, Int. J. Optoelectron. **5**, 405 (1990).
[11] T. D. Dudderar, R. Meynart, and P. G. Simpkins, Opt. Lasers Eng. **9**, 211 (1988).
[12] R. D. Keane and R. J. Adrian, Meas. Sci. Technol. **1**, 1202 (1990).
[13] P. T. Callaghan, *Principles of NMR Microscopy* (Clarendon Press, Oxford, 1991).
[14] B. Blümich, *NMR Imaging of Materials* (Clarendon Press, Oxford, 2000).
[15] W. A. Edelstein *et al.,* Phys. Med. Biol. **25**, 751 (1980).
[16] E. Fukushima, Annu. Rev. Fluid Mech. **31**, 95 (1999).